JOURNAL OF SOLID STATE CHEMISTRY 118, 125–132 (1995)

Oxygen Ion Migration in Perovskite-Type Oxides

M. Cherry,*,† M. S. Islam,*,[1] and C. R. A. Catlow†

*Department of Chemistry, University of Surrey, Guildford, GU2 5XH, United Kingdom; and †Davy-Faraday Laboratories, The Royal Institution, 21 Albemarle Street, London W1X 4BS, United Kingdom

Received October 28, 1994; in revised form February 7, 1995; accepted February 9, 1995

Computer simulation techniques have been applied to perovskite-structured $LaBO_3$ (where B = Cr, Mn, Fe, Co) in order to elucidate the mechanistic features and energetics of oxygen ion migration. For the four compounds considered, a common set of interatomic potentials was derived that correctly reproduces their observed cubic structures. The results support models in which diffusion is mediated by oxygen ion vacancies. Analysis of the potential energy surface demonstrates that vacancy migration takes place along the anion octahedron edge, although not in a linear fashion but via a curved path. The calculated migration energies vary from 0.5 to 0.9 eV and are in accord with the available experimental values. We consider the relationship between the cation size and the migration energy, which was investigated by modifying the interatomic potential function to relate ionic radii directly to the short-range repulsive term. We also examine the energies of solution for alkaline-earth dopants on the La site with oxygen vacancy compensation. Ion size effects are found to be important, with Sr calculated to have the highest solubility. Finally, we investigate the formation of dopant–vacancy pair clusters. © 1995 Academic Press, Inc.

1. INTRODUCTION

The perovskite-type oxides based on the general formula $LaBO_3$ (where B = Cr, Mn, Fe, Co) comprise a rich family of compounds with important applications in solid oxide fuel cells (1–4) and in oxidation catalysis (5–10). It is recognized that the defect chemistry and the facile diffusion of oxygen are vital in controlling their physical properties (e.g., electrical conductivity, catalytic activity). Consequently, the importance of understanding the ion transport behavior in these materials has resulted in numerous studies of oxygen diffusion (11–18), employing a variety of techniques such as ac/dc ionic conductivity, secondary ion mass spectrometry (SIMS), and potentiostatic step methods.

Typically, these materials are doped on the La^{3+} site with aliovalent ions (e.g., Sr^{2+}), which leads to charge compensation by the formation of ionic and electronic defects. The type of defect depends upon the nature of the dopant, the oxygen partial pressure, and the temperature. At low oxygen pressure (or low oxygen activity) the predominant defect in $La_{1-x}Sr_xBO_3$ are oxygen ion vacancies (3, 16, 19).

A few studies have attempted to develop a framework to identify perovskite-type materials with high ionic conductivity. For example, Cook and Sammells (20) have proposed various criteria for selecting new solid electrolytes, such as lattice "free volume" and the critical radius of the opening at the migration saddle point. In addition, computer simulations have demonstrated that the low-vacancy migration energies in fluorite-type oxygen ion conductors are due to a balance between several factors, principally electrostatic, short-range, and polarization energies (21).

It is clear that for a full understanding of oxygen transport in perovskite-type oxides, it is important to examine the mechanisms of diffusion, as well as the relationship between the ion size and the activation energy. However, despite the several studies referred to above, fundamental mechanistic features are still uncertain. It is known that the results from experimental studies are rarely sufficient to identify fully the migration mechanism. We have therefore used computer simulations to clarify some of the factors controlling oxygen transport in $LaBO_3$; our work extends previous studies by Kilner and Brook (13) of the lanthanide aluminates ($LnAlO_3$). These simulation techniques are particularly suited to probing ion migration on the atomic scale and have been successfully applied to analogous problems in solid oxide catalysts (22–24) and perovskite-based cuprate superconductors (25–28). In this work we have explored various mechanisms or pathways for oxygen migration, as well as trends in migration energy as a function of cation size.

2. METHODOLOGY AND POTENTIALS

The simulation techniques are based upon energy minimization procedures and a Mott–Littleton methodology for accurate modeling of perfect and defective lattices.

[1] To whom correspondence should be addressed.

0022-4596/95 $12.00

Detailed reviews of these well-established computational methods are given elsewhere (29, 30).

An important feature of these calculations is the treatment of lattice relaxation about the point defect or migrating ion. The Mott–Littleton approach is to partition the crystal lattice into two regions so that ions in a spherical inner region surrounding the defect are relaxed explicitly. In contrast, the remainder of the crystal, where the defect forces are relatively weak, is treated by more approximate quasi-continuum methods. In this way local relaxation is effectively modeled and the crystal is not considered simply a rigid lattice through which ion species diffuse.

There is now ample evidence that given reliable interatomic potentials and a sufficiently large inner region these methods can produce accurate values of the energies of defect formation, migration, and substitution (21–28). The potentials describing the interatomic interactions are represented by ionic, pair-wise potentials of the form

$$\phi_{\alpha\beta}(r) = \frac{-Z_\alpha Z_\beta e^2}{r} + A_{\alpha\beta}\exp(-r/\rho_{\alpha\beta}) - C_{\alpha\beta}/r^6, \quad [1]$$

which includes the long-range Coulombic term and an analytical function to model overlap–repulsions and van der Waals forces. Because charged defects will polarize other ions in the lattice, ionic polarizability must be incorporated into the potential model. The shell model (31) provides a simple description of such effects by treating each ion in terms of a core (representing the nucleus and core electrons) connected via a harmonic spring to a shell (representing the valence electrons). Shell model potentials have proven to be effective in simulating the dielectric properties of ceramic oxides.

The short-range potential parameters assigned to each ion–ion interaction were derived by empirical fitting to observed structural properties. The LaBO$_3$ compounds adopt the ideal cubic perovskite structure (shown in Fig. 1) at the elevated temperatures at which diffusion experiments are typically carried out. For all four compounds considered, namely $LaCrO_3$, $LaMnO_3$, $LaFeO_3$, and $LaCoO_3$, the potential parameters for the $La^{3+}\cdots O^{2-}$ and $O^{2-}\cdots O^{2-}$ interactions were fitted simultaneously, resulting in a common set of interatomic potentials. This approach enables some information concerning the curvature of the energy surface to be included and has the added advantage of improved transferability. The methodology of fitting to multiple lattices has been implemented in the program GULP (32). The potentials and shell model parameters used in this study are listed in Table 1. We note that our pair-potentials were found to be more appropriate for the present study than the alternative set reported recently by Bush *et al.* (33); their potentials, although excellent for modeling perfect lattices of metal oxides, were not explicitly designed for defects in the LaBO$_3$ systems.

Prior to carrying out the migration calculations, the unit cell dimensions and ion positions are equilibrated under constant pressure conditions. The calculated bond distances and lattice parameters and their comparison with experimental values are listed in Table 2. Examination of the differences shows a good agreement between experimental and simulated structures. Unfortunately, there are no additional experimental data on dielectric and elastic properties which would be useful for further validation and refinement of the potential model.

TABLE 1
Interatomic Potentials for the LaBO$_3$ Perovskites

(i) Short-range

Interaction	A (eV)	ρ (Å)	C (eV Å^{-6})
$La^{3+}\cdots O^{2-}$	1545.21	0.3590	0
$Cr^{3+}\cdots O^{2-}$	1690.90	0.3010	0
$Mn^{3+}\cdots O^{2-}$	1267.50	0.3214	0
$Fe^{3+}\cdots O^{2-}$	1156.36	0.3299	0
$Co^{3+}\cdots O^{2-}$	1329.82	0.3087	0
$O^{2-}\cdots O^{2-}$	22764.3	0.1490	43.0

(ii) Shell model[a]

Species	Y (e)	k (eV Å^{-2})
La^{3+}	−0.25	145.0
Cr^{3+}	0.97	67.0
Mn^{3+}	3.00	95.0
Fe^{3+}	4.97	304.7
Co^{3+}	2.04	196.3
O^{2-}	−2.24	42.0

[a] Y and k refer to the shell charge and harmonic force constant, respectively.

Note. Potential cutoff, 3.0 lattice units; Region I, 250 ions.

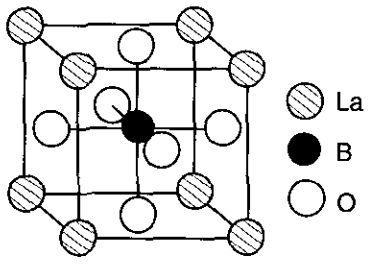

FIG. 1. Cubic perovskite structure for a LaBO$_3$ oxide.

TABLE 2
Calculated and Experimental Structural Parameters for the Cubic Perovskites

Compound	Lattice constants a_0^{obs} (Å)	a_0^{calc} (Å)
$LaCrO_3$	3.874	3.874
$LaMnO_3$	3.904	3.904
$LaFeO_3$	3.926	3.926
$LaCoO_3$	3.820	3.823

Compound	Interatomic separations Separation	r_{obs} (Å)	r_{calc} (Å)
$LaCrO_3$	La–O	2.7393	2.7394
	Cr–O	1.9370	1.9370
	O–O	2.7393	2.7394
$LaMnO_3$	La–O	2.7605	2.7605
	Mn–O	1.9520	1.9520
	O–O	2.7605	2.7605
$LaFeO_3$	La–O	2.7761	2.7761
	Fe–O	1.9630	1.9630
	O–O	2.7761	2.7761
$LaCoO_3$	La–O	2.7011	2.7029
	Co–O	1.9100	1.9113
	O–O	2.7011	2.7029

3. RESULTS AND DISCUSSION

3.1. Migration Mechanism and Energetics

Although, as noted, there have been several reports on oxygen diffusion in $LaBO_3$ materials (11–18), the amount of information on migration activation energies and fundamental mechanistic features is rather limited. It is generally accepted that oxygen diffusion is based on rapid transport of vacancies which migrate by a conventional hopping mechanism, although this has not been confirmed by experiment.

We have investigated these problems by an extensive search of the potential energy surface. The energy profiles are mapped out by calculating the defect energy of the migrating ion along the diffusion path, and allowing relaxation of the lattice at each position. In this way the saddle-point configuration can be identified from which the energy barrier to migration is derived. An example of an energy profile is shown in Fig. 2. The resulting activation energies are reported in Table 3 together with the available values from experiment.

Examination of the results confirms migration of oxygen ion vacancies as the lowest energy path. The calculated values accord well with experimental activation energies, although direct comparison is not straightforward since the observed values show significant variation. This scatter may reflect differences in experimental conditions and oxygen stoichiometry, as well as problems with phase purity. We should note that the calculated energies in Table 3 relate to intrinsic migration of oxygen defects and do not include formation or association energy terms, a point to which we return below.

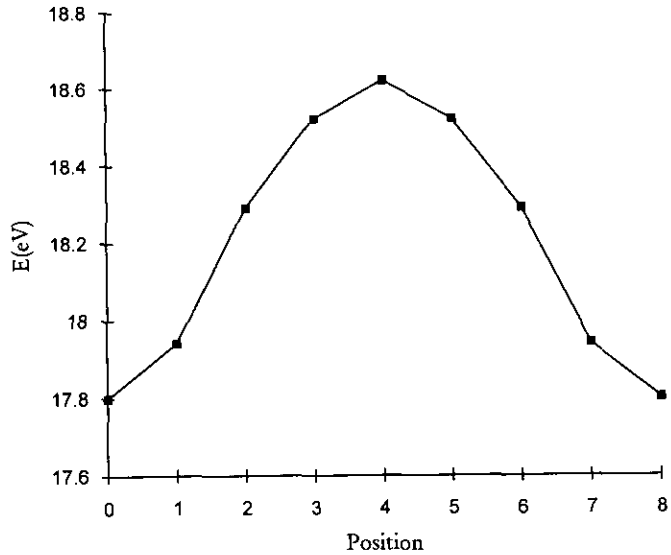

FIG. 2. Energy profile for vacancy migration between nearest-neighbor anions in $LaMnO_3$. The points indicate calculated energies at equidistant positions along the migration path.

The location of ions and the available space in the perovskite lattice suggest that interstitial diffusion is unlikely. This is confirmed by our defect calculations, which find high energy barriers (>1.5 eV) to interstitial migration. For comparison, the corresponding energy for interstitial migration in fluorite-structured ThO_2 is about 0.9 eV (21, 30). Hence, our results confirm that ion diffusion in perovskite-type $LaBO_3$ arises from the mobility of oxygen ion vacancies.

TABLE 3
Migration Activation Energies

Compound	E_m^{calc} (eV)	E_m^{expt} (eV)
$LaCrO_3$	0.48	—
$LaMnO_3$	0.86	0.73[a]
$LaFeO_3$	0.50	0.77 ± 0.25[b]
$LaCoO_3$	0.61	0.62 ± 0.21,[c] 0.78 ± 0.22[d]

[a] Belzner *et al.* (16).
[b] Ishigaki *et al.* (12).
[c] Carter *et al.* (15).
[d] Ishigaki *et al.* (11).

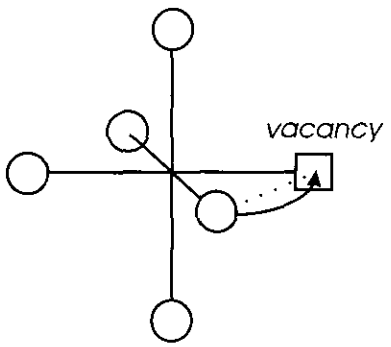

FIG. 3. Schematic representation of the curved path for oxygen vacancy migration along the BO_6 octahedron edge.

An important result of our search of the potential energy surface is that we find a small deviation from the direct path for vacancy migration; this is shown schematically in Fig. 3 and as a contour map in Fig. 4. It has commonly been assumed that the migrating ion takes a direct linear path long the ⟨110⟩ edge of the BO_6 octahedra into an adjacent vacancy, for which the saddle point is located midway between the two anion sites. However, the calculations reveal a curved route with the saddle point away from the neighboring B site cation, resulting in a significantly lower energy barrier to oxygen migration. The magnitude of this deviation for each $LaBO_3$ compound is shown in Fig. 5 and listed in Table 4. A clear trend with B site radius does not emerge, partly due to the small range of cation sizes investigated. Nevertheless, the greatest deviation corresponds to the largest cation at the B site.

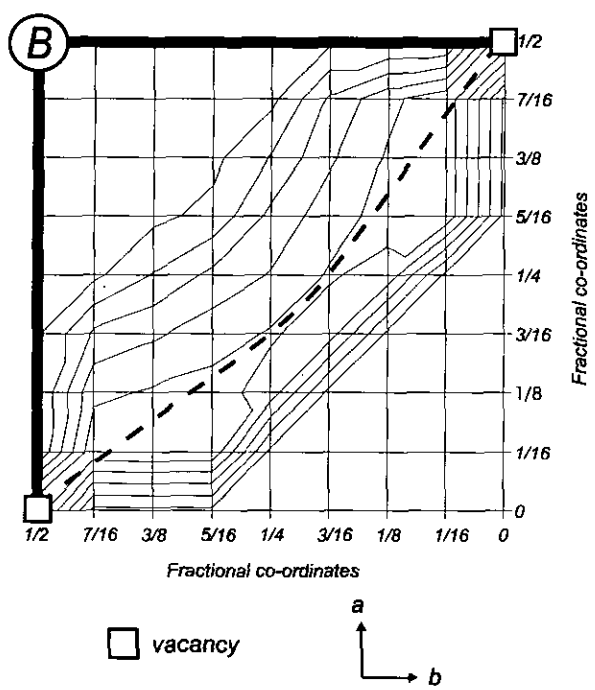

FIG. 4. Contour plot of the potential energy surface for oxygen vacancy migration, showing the curved path between adjacent anion sites of a BO_6 octahedron (in the ab plane).

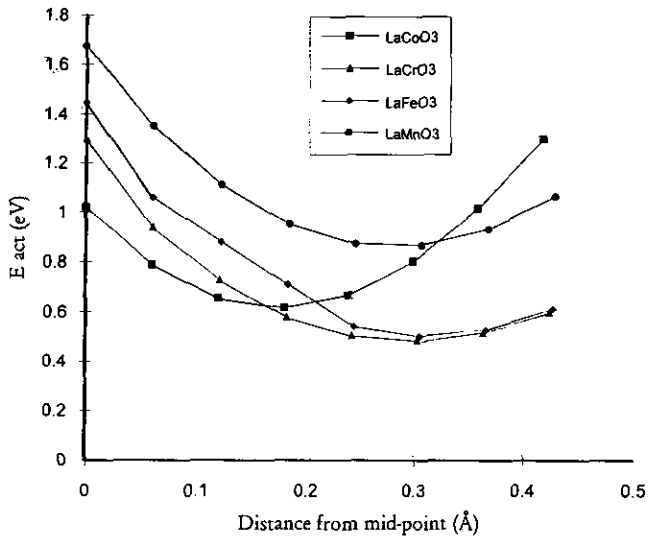

FIG. 5. Migration energy as a function of the ion position normal to the midpoint of a linear path between nearest-neighbor anions.

In the saddle-point configuration, the migrating ion must pass through the opening of a triangle defined by two A site (La^{3+}) ions and one B site ion (Fig. 6). Clearly the repulsive interactions can be reduced by the outward movement of the nearest cations. The simulation approach is able to model lattice relaxation and generate valuable information on local ion movements. It is worth recalling that ionic polarizability has been treated in our simulations by the shell model. Therefore, the crystal structure is not considered simply a hard-sphere lattice with fixed ions. From our analysis we find average displacements of the La^{3+} and B^{3+} ions of 0.08 and 0.07 Å, respectively, away from the mobile oxygen ion (shown in Fig. 6). These results emphasize that neglecting lattice

TABLE 4
Deviation from Direct Linear Path for Vacancy Migration

Compound	B radius (Å)[a]	Deviation (Å)[b]
$LaCrO_3$	0.61	0.42
$LaMnO_3$	0.65	0.43
$LaFeO_3$	0.65	0.43
$LaCoO_3$	0.61	0.25

[a] Shannon and Prewitt (34).
[b] Deviation of the saddle point from the linear path (shown in Figs. 4 and 5).

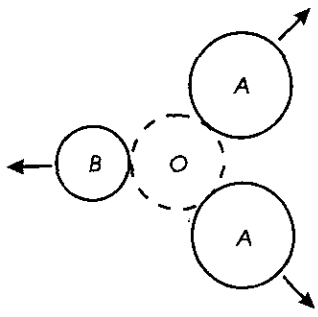

FIG. 6. Saddle-point configuration for oxygen ion migration, indicating the cation relaxation.

relaxation effects at the saddle point may be a serious flaw in previous ion size approaches based on a rigid hard-sphere model, in which the "critical radius" of the opening is derived (20).

3.2 Variation in Ion Size

It is clear that the size proportion of the A and B cations in the perovskite structure is an important factor for high ionic conductivity. A geometric analysis of the saddle-point configuration, as illustrated by Fig. 6, has been employed before in the context of defining selection criteria for good ion conductors (20). Here we further examine the relationship between migration energy and cation size within our simulation procedure.

Our approach is to change systematically our interatomic potential model so as to calculate the vacancy migration energy as a direct function of the ionic size of the A and B cations. To model ion-size changes we vary the exponential Born–Mayer function (Eq. [1]) which enables the short-range repulsive energy to be related to ionic radii, as suggested by Fumi and Tosi (35). The forms of the potentials are

$$V_{A\text{-}O} = A \exp[(r_A + r_O)/\rho] \quad [2]$$

$$V_{B\text{-}O} = A \exp[(r_B + r_O)/\rho], \quad [3]$$

where r_A, r_B, and r_O are the ionic radii of the A cation, B cation, and oxygen ion, respectively.

Using these potentials we were able to calculate the migration energies, illustrated in Fig. 7, of the vacancy jump for a range of A and B cation radii. The starting point in each case corresponds to the parameters for the $LaMnO_3$ system, where the size of A is varied, with B fixed at the Mn^{3+} radius (0.65 Å) and similarly, the size of B is varied, with the A value set at La^{3+} (1.06 Å).

The results indicate two main points. First, the calculations exhibit a clear trend toward lower migration energies with smaller A site cations. There is an optimum value of about 0.95 Å, below which the migration energy rises steeply. This is in accord with the limited amount of experimental evidence and with results of similar calculations on lanthanide aluminates ($LnAlO_3$) (13). Second, as is evident from Fig. 7b, there is a decrease in energy with increasing size of the B cation, with a minimum at 0.75 Å. However, the plot also shows a discontinuity at about 0.55 Å. A likely explanation is that this reflects the B cation size approaching the tolerance limit for a stable perovskite structure. Indeed, our lattice dynamics calculations are consistent with this veiw as they reveal the presence of negative phonon frequencies at this point, which indicates a structural instability.

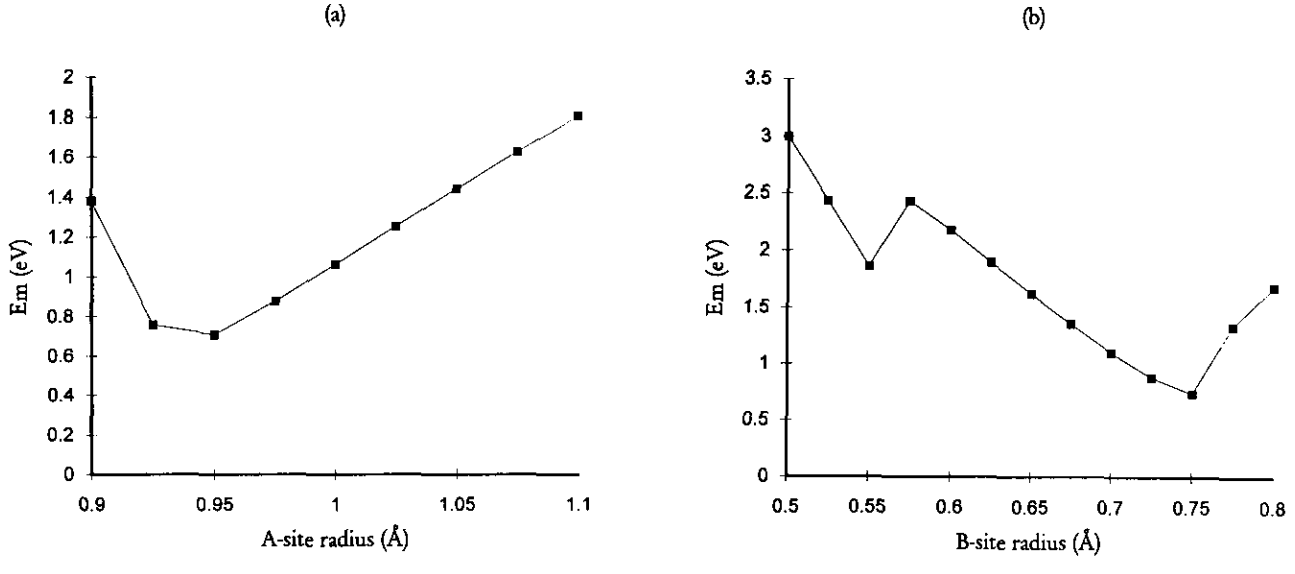

FIG. 7. Calculated migration energy as a function of cation size (a) at the A site (b) at the B site.

It is well established that simple geometrical limits for cation radii on the A and B sites can be defined by the so-called Goldschmidt Tolerance Factor, given by

$$t = (r_A + r_O)/\sqrt{2}\,(r_B + r_O), \qquad [4]$$

where we note that, nominally, the perovskite structure is stable for $1.0 > t > 0.75$. To assess our results further, we consequently examined the relationship between the tolerance factor and our calculated migration energies. The result is illustrated in Fig. 8. As can be seen, a degree of correlation exists with a clear minimum at $t = 0.81$. Using ionic radii from Shannon and Prewitt (34) we derive, for example, a t value of 0.85 for $LaMnO_3$ which is the most commonly used cathode material in fuel cell technology. Our calculations, therefore, suggest that materials with a t value of about 0.81 may lead to lower migration energies and faster diffusion, a result with practical consequences for oxidation catalysis and for operating fuel cells at lower temperatures and at higher rates. By using the same set of radii, we find that this value of the tolerance factor would encompass various perovskite electrolytes, such as $PrMnO_3$ and $GdMnO_3$.

We can attempt to rationalize our results in terms of lattice relaxation effects. As the mobile oxygen ion approaches the saddle point it must pass through the center of a triangle of cations (shown in Fig. 6). Our calculations have already shown that the repulsive overlap interactions can be reduced by the outward relaxation of these cations. It appears that the *minimum* in the tolerance factor corresponds to the most effective balance of the relaxation of the A and B cations at the saddle-point position. In other words, the even distribution of relaxation between the cations is an important factor for low energy barriers to oxygen ion migration.

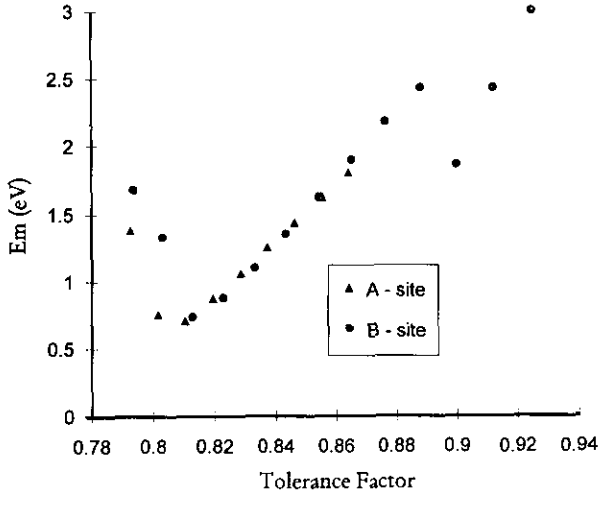

FIG. 8. Calculated migration energy as a function of the tolerance factor (from both the A and B site simulations).

TABLE 5
Energies of Solution for Alkaline-Earth Dopants with Oxygen Vacancy Compensation

Compound	E_{sol} (eV/dopant)			
	Mg^{2+}	Ca^{2+}	Sr^{2+}	Ba^{2+}
$LaCrO_3$	4.35	1.06	0.37	3.97
$LaMnO_3$	4.20	0.73	−0.01	3.53
$LaFeO_3$	3.92	0.35	−1.17	2.31
$LaCoO_3$	4.60	1.54	1.18	5.26

3.3. Dopant Ion Substitution

It has been widely shown that the addition of dopant ions to the $LaBO_3$ oxides is crucial to promoting catalytic activity and high conductivity (1–10). These materials are commonly "acceptor" doped with low-valent cations (e.g., Sr^{2+}) which substitute for La^{3+}; this reduction of the effective valence of the A site cations leads to the formation of a compensating population of oxygen vacancies at low oxygen partial pressures. The increased oxygen vacancy concentration gives rise to the observed high ionic conductivity. The corresponding substitution reaction can be represented by the following defect equation for alkaline-earth dopants:

$$MO + La_{La}^{x} \rightarrow M'_{La} + \tfrac{1}{2}V_O^{\cdot\cdot} + \tfrac{1}{2}La_2O_3.$$

The energies of this "solution" reaction can be evaluated by our simulation approach in which we combine appropriate defect and lattice energy terms. Our calculated energies of solution for alkaline-earth dopants are presented in Table 5 and are also shown as a function of ion radius in Fig. 9. The interatomic potentials for the dopant species are exactly those of the corresponding alkaline-earth metal oxides (36) which have been successfully applied to similar studies of dopant substitution in the $YBa_2Cu_3O_7$ superconductor (26) and the La_2O_3 methane coupling catalyst (22).

Examination of the results reveals that the most favorable solution energy and hence the highest solubility is predicted for Sr^{2+} in all the $LaBO_3$ hosts. This is clearly illustrated in Fig. 9 which shows a strong correlation between the solution energy and the dopant size with a minimum at Sr^{2+} (close to the La^{3+} radius of 1.06 Å). Our results accord well with experimental studies which have demonstrated how the addition of Sr (and, to a lesser extent, Ca) leads to an increase in the oxygen diffusion

coefficient and to high catalytic activity. The calculations also show that solution of MgO and BaO is appreciably endothermic, in line with the observed low solubility.

3.4. Dopant–Vacancy Clusters

It is well established that for the fluorite-structured ion conductors, such as Y-doped CeO_2, the conductivity is controlled by the extent of dopant–vacancy interactions (30, 37). These can be described in terms of the formation of simple pair clusters for low dopant concentrations, which add a binding energy term to the Arrhenius energy of the ionic conductivity. Both experiment and calculations have shown that the elastic strain interaction between the dopant and the oxygen vacancy is at least as important as the electrostatic term (13, 30, 37).

Consequently, we have considered pair clusters in the $LaBO_3$ systems comprised of nearest-neighbor dopant substitutionals and oxygen vacancies. We have already found the solution of Sr more favorable than that of other cations; moreover, Sr is the most commonly used dopant for the $LaBO_3$ hosts. We will therefore focus our attention on the formation of Sr-vacancy clusters. The calculated binding energies with respect to the component isolated defects are reported in Table 6.

The results reveal that the pair cluster is bound only in the $LaCoO_3$ material which would inhibit the oxygen mobility in this system. These results suggest that, with the exception of $LaCoO_3$, there will be little tendency toward clustering at low dopant concentrations, although it is possible that other types of aggregates could have greater stability. We recall that our calculated migration energies accord well with the experimental activation energies.

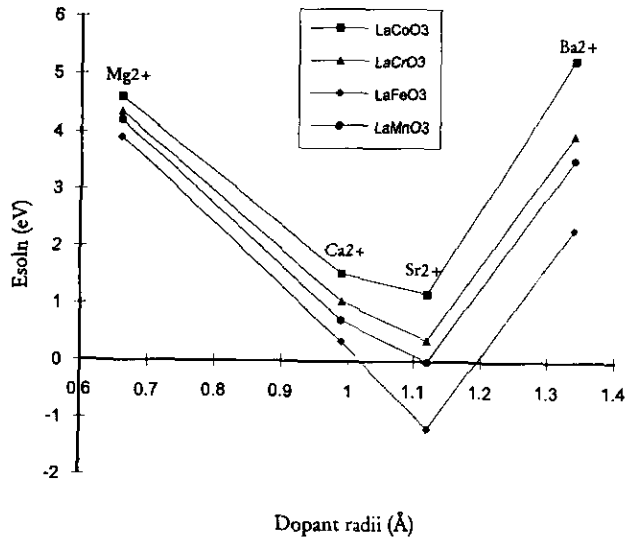

FIG. 9. Calculated energies of solution as a function of ionic radius for alkaline-earth dopants.

TABLE 6
Binding Energies for Sr–Oxygen Vacancy Pair Clusters and Calculated Static Dielectric Constants

Compound	E_b (eV)	ε_0
$LaCrO_3$	0.03	36.4
$LaMnO_3$	0.35	56.1
$LaFeO_3$	1.10	105.0
$LaCoO_3$	−0.19	23.0

This may indicate that binding energy terms are not significant in these materials at low dopant content, a view that is consistent with our cluster calculations.

It is interesting to note that we find a strong correlation between the binding energy and the calculated static dielectric constant, which suggests that screening effects are important. The most favorable binding energy is calculated for $LaCoO_3$, which also has the lowest value for the dielectric constant (Table 6). While we have included all of the key terms, we should note, however, that there are uncertainties in the absolute values of the binding energies due to their sensitivity to the choice of O–O potential parameters. Nevertheless, our main concern here is to understand how defect clusters may form; for this task our modeling procedures have proved to be reliable.

4. CONCLUSION

The present study demonstrates how computer modeling techniques can be used to examine oxygen transport properties in perovskite-type oxides that are relevant to their use in oxidation catalysis, fuel cells, and separation membranes. It is clear that analogous modeling procedures could be applied to other nonstoichiometric systems, including the oxides of the general type ABO_{3-x}. The following conclusions have emerged from our discussion.

(1) Diffusion is mediated by hopping of oxygen-ion vacancies along the anion octahedra edge, but not in a linear fashion; rather migration takes place via a curved path, resulting in a significantly lower energy barrier. Our calculated migration energies are in accord with the available experimental data.

(2) The calculations demonstrate the importance of lattice relaxation effects at the migration saddle point, which were previously neglected by ion size arguments based on a simple hard-sphere approach.

(3) We find a clear trend toward lower migration energies with smaller A site cations and larger B site cations. The calculations also exhibit a strong relationship be-

tween our calculated migration energy and the perovskite tolerance factor.

(4) Ion size effects are found to be important for dopant substitution, with Sr calculated to have the most favorable solution energy. This is in agreement with experimental results which show the highest oxygen diffusion and catalytic activity for Sr-doped $LaBO_3$. The binding energies indicate that there is little tendency toward pair cluster formation except for $LaCoO_3$.

The present study of bulk transport will be extended to encompass surface properties and in particular the surface exchange of oxygen.

ACKNOWLEDGMENTS

This work was supported by the EPSRC and BP Research and Engineering. We are also grateful for useful discussions with J. A. Kilner, S. Ramdas, J. D. Gale, and T. S. Bush.

REFERENCES

1. B. C. H. Steele *in* "Proceedings, International Symposium on Solid Oxide Fuel Cells" (O. Yamamoto, M. Dokiya, and H. Tagawa, Eds.), Science House, Tokyo, 1990.
2. N. Q. Minh, *J. Am. Ceram. Soc.* **76,** 563 (1993).
3. H. U. Anderson, *Solid State Ionics* **52,** 33 (1992).
4. O. Yamamoto, Y. Takeda, R. Kanno, and M. Noda, *Solid State Ionics* **22,** 241 (1987).
5. L. G. Tejuca, J. L. G. Fierro, and J. M. D. Tascon, *Adv. Catal.* **36,** 237 (1989).
6. N. Yamazoe and Y. Teraoka, *Catal. Today* **8,** 175 (1990).
7. J. G. McCarty and H. Wise, *Catal. Today* **8,** 231 (1990).
8. C. B. Alcock, J. J. Carberry, R. Doshi, and N. Gunasekaran, *J. Catal.* **143,** 533 (1993).
9. P. Salomonsson, T. Griffin, and B. Kasemo, *Appl. Catal. A* **104,** 175 (1993).
10. P. E. Marti and A. Baiker, *Catal. Lett.* **26,** 71 (1994).
11. T. Ishigaki, S. Yamauchi, J. Mizusaki, K. Fueki, and H. Tamura, *J. Solid State Chem.* **54,** 100 (1984).
12. T. Ishigaki, S. Yamauchi, K. Kishio, J. Mizusaki, and K. Fueki, *J. Solid State Chem.* **73,** 179 (1988).
13. J. A. Kilner and R. J. Brook, *Solid State Ionics* **6,** 237 (1982).
14. J. Mizusaki, *Solid State Ionics* **52,** 79 (1992).
15. S. Carter, A. Selcuk, R. J. Chater, J. Kajda, J. A. Kilner, and B. C. H. Steele, *Solid State Ionics* **53–56,** 597 (1992).
16. A. Belzner, T. M. Gür, and R. A. Huggins, *Solid State Ionics* **57,** 327 (1992).
17. C. B. Alcock, R. C. Doshi, and Y. Shen, *Solid State Ionics* **51,** 281 (1992).
18. T. Inoue, J. Kamimae, M. Ueda, K. Eguchi, and H. Arai, *J. Mater. Chem.* **3,** 751 (1993).
19. A. Reller, *Philos. Mag. (Part) A* **68,** 641 (1993).
20. R. L. Cook and A. F. Sammells, *Solid State Ionics* **45,** 311 (1991).
21. C. R. A. Catlow, *J. Chem. Soc. Faraday Trans.* **86,** 1167 (1990).
22. D. J. Ilett and M. S. Islam, *J. Chem. Soc. Faraday Trans.* **89,** 3833 (1993).
23. M. S. Islam, D. J. Ilett, and S. C. Parker, *J. Phys. Chem.*, **98,** 9637 (1994).
24. C. R. A. Catlow, R. A. Jackson, and J. M. Thomas, *J. Phys. Chem.* **94,** 7889 (1990).
25. M. S. Islam and R. C. Baetzold, *J. Mater. Chem.* **4,** 299 (1994).
26. M. S. Islam, *Molec. Sim.* **12,** 101 (1994).
27. M. S. Islam and C. Ananthamohan, *J. Solid State Chem.* **100,** 371 (1992).
28. N. L. Allan and W. C. Mackrodt, *Philos. Mag. Part A* **64,** 1129 (1991).
29. A. K. Cheetham and P. Day (Eds.), "Solid State Chemistry—Techniques" Chap. 7, Clarendon, Oxford, 1987.
30. C. R. A. Catlow, *Solid State Ionics* **8,** 89 (1983).
31. B. J. Dick and A. W. Overhauser, *Phys. Rev.* **112,** 90 (1958).
32. J. D. Gale, "GULP (General Utility Lattice Programme)," Royal Institution, London, 1993, to be published.
33. T. S. Bush, J. D. Gale, C. R. A. Catlow, and P. D. Battle, *J. Mater. Chem.* **4,** 831 (1994).
34. R. D. Shannon and C. T. Prewitt, *Acta Crystallogr. Sect. B* **25,** 925 (1969); *Acta Crystallogr. Sect.* **26,** 1049 (1970).
35. F. G. Fumi and M. P. Tosi, *J. Phys. Chem. Solids* **25,** 31 (1964).
36. G. V. Lewis and C. R. A. Catlow, *J. Phys.* **6,** 18, 1149 (1985).
37. R. Gerhardt-Anderson and A. S. Nowick, *Solid State Ionics* **5,** 547 (1981).